ELSEVIER

Contents lists available at ScienceDirect

# **Surface & Coatings Technology**

journal homepage: www.elsevier.com/locate/surfcoat



# Effects of nanoscale chemical heterogeneity on the wear, corrosion, and tribocorrosion resistance of Zr-based thin film metallic glasses



Wenbo Wang<sup>a</sup>, Hesham Mraied<sup>b</sup>, Wahyu Diyatmika<sup>c</sup>, Jinn P. Chu<sup>c,d</sup>, Lin Li<sup>e</sup>, Wenjun Cai<sup>a,\*</sup>

- <sup>a</sup> Department of Materials Science and Engineering, Virginia Polytechnic Institute and State University, VA 24061, United States
- b Department of Civil and Environmental Engineering, University of South Florida, Tampa 33620, FL, United States
- <sup>c</sup> Department of Materials Science and Engineering, National Taiwan University of Science and Engineering, Taipei 10607, Taiwan
- <sup>d</sup> Applied Research Center for Thin-Film Metallic Glass, National Taiwan University of Science and Technology, Taipei 10607, Taiwan
- <sup>e</sup> Department of Metallurgical and Materials Engineering, The University of Alabama, Tuscaloosa, AL 35487, United States

#### ARTICLE INFO

#### Keywords: Thin film metallic glass Chemical heterogeneity Corrosion Wear Tribocorrosion

#### ABSTRACT

The effects of nanoscale chemical heterogeneity on the wear, corrosion, and tribocorrosion resistance of ZrCuNiAl thin film metallic glasses were investigated by examining samples of similar global composition but with either homogenous or heterogeneous local composition. Unlike the homogenous sample, the heterogeneous sample exhibited local compositional fluctuations of Zr-rich ( $\sim$ 52.8 at.%) and Zr-lean ( $\sim$ 51.7 at.%) regions separated by  $\sim$ 413.0  $\pm$  64.7 nm. Dry scratch wear study showed that the homogenous samples exhibited lower wear rates and friction coefficients than their heterogenous counterparts due to their higher hardness and lower stiffness, as measured from nanoindentation tests. Corrosion resistance of both samples was studied through potentiodynamic polarization and Mott-Schottky analysis in 0.6 M NaCl aqueous solution under room temperature. It was found that the heterogeneous samples exhibited higher pitting resistance than their homogenous counterparts by forming a protective passive layer with lower defect density. Finally, the effects of chemical heterogeneity on the tribocorrosion rate and repassivation kinetics of both samples were discussed based on their differences in mechanical and electrochemical properties measured.

#### 1. Introduction

Metallic glasses (MGs) exhibit good elastic limit [1], high strength [2,3], and excellent wear [4,5] and corrosion resistance [6,7] largely owing to the lack of long-range order, the absence of grain boundary, and in many cases, the retention of high alloying content in homogenous solid solution [8,9]. With the reduction of the critical cooling rate, MGs can be cast into bulk metallic glasses (BMGs) to optimize mechanical properties such as strength and fracture toughness, however, they often suffer from a very limited ductility and serrated plastic flow [9-12]. Thin film metallic glasses (TFMGs), i.e. MGs with typically hundreds of nanometers to several microns thickness, offset the shortcomings of BMGs by retarding strain localization via interface-mediated plasticity and hence have drawn great interest lately as they can be readily applied as coatings for various engineering applications which requires both good mechanical properties and high corrosion resistance on the surface [13-15]. For instance, Pd-based TFMGs with attractive forming ability have been used in micro-electro-mechanical systems (MEMS) [16]. Zr-based TFMGs, the focus of this work, have been

applied in dental implant due to their high strength, exceptional fracture toughness and corrosion resistance [17]. In many of these applications, simultaneous wear and corrosion resistance, i.e. tribocorrosion resistance, are essential for the product's long-term durability and safe operation.

The hardness of Zr-based TFMGs prepared by physical vapor deposition ranges from  $\sim\!5.5$  GPa to as high as  $\sim\!16.2$  GPa at room temperature [18–20]. Such high hardness typically translates into wear resistance superior to many conventional engineering metals in various applications [21,22]. For example, Tsai et al. found that the cutting durability of surgical blades coated with Zr<sub>48</sub>Cu<sub>36</sub>Al<sub>8</sub>Ag<sub>8</sub> and Zr<sub>53</sub>Cu<sub>30</sub>Ni<sub>9</sub>Al<sub>8</sub> TFMGs was much higher than that of commercial AISI 440C martensitic stainless steel [23]. Cai et al. showed that the fretting wear rate of Zr<sub>60.14</sub>Cu<sub>22.31</sub>Fe<sub>4.85</sub>Al<sub>9.7</sub>Ag<sub>3</sub> TFMGs was approximately 2.8 times lower than that of Ti6Al4V alloys under the same dry sliding conditions [17]. However, since wear of Zr-based TFMGs is a complex dynamic process, often associated with subsurface shear band formation and contingent crystallization [24], the opposite has also been reported [25]. For example, Fu et al. [25] studied the sliding behavior

E-mail address: caiw@vt.edu (W. Cai).

<sup>\*</sup> Corresponding author.

of Zr-based MGs using molecular dynamics simulation and found that no exceptional friction and wear characteristics were observed.

A recently proposed four R's design paradigm has pointed out the importance of tailoring the properties of MGs via controlling their nanoscale compositional and structural heterogeneity [26,27], where the four R's represent (1) retaining more soft spots that participate in soft vibrational modes, (2) restraining shear-band propagation and nucleation, (3) rejuvenating glass structure into a more deformable state, and (4) relocating to alloy compositions rich in structural inhomogeneity. Based on such hypothesis, the macroscopic properties of MGs can be tailored by tuning the nanoscale chemical heterogeneity during processing. Indeed, several experimental and simulation studies of BMGs and TFMGs have indicated that nanoscale heterogeneity strongly affects both of their mechanical and corrosion properties [28-30]. It should also be pointed out that while MGs are inherently inhomogeneous with a wide spectrum of atomic-packing heterogeneities, the term 'nanoscale heterogeneity' used herein specifically refers to quasi-periodic compositional fluctuations over a length scale of hundreds of nanometers, hence a higher degree of heterogeneity than those intrinsic to conventional homogenous MGs. For example, Rashidi et al. [28] reported that the chemical heterogeneity was induced during the introduction of Sn to Cu<sub>47</sub>Zr<sub>47</sub>Al<sub>6</sub> bulk metallic glass, resulting in increased shear band formation and enhanced ductility. Wang et al. [29] studied the effects of nanoscale chemical heterogeneity on the mechanical properties of Cu-Zr MGs via multiscale computer simulation and found that the organization of nanometer-scale shear transformation into shear-band patterns is dependent on the length-scale of the spatial heterogeneity. An optimum correlation length of ~5 nm was identified to result in the highest plastic strain to failure and lowest strain localization.

In terms of corrosion resistance, the chemical heterogeneity is often found to exhibit an adverse effect on the corrosion resistance of MGs owing to its obstruction to uniform passive film growth [31]. Zhang et al. [30] found that the Al<sub>3</sub>Ni or Al<sub>11</sub>Ce<sub>3</sub> intermetallics precipitation has negative effect on pitting resistance of Al-based MG whereas no detrimental effect was observed in nanoscale  $\alpha$ -Al precipitation. Mudali et al. [32] pointed out that chemical inhomogeneous cluster zones in Zr-based BMGs served as attractive sites for aggressive ions and further accelerate the corrosion in locations containing less noble alloy components. Generally speaking, chemical homogeneity and an absence of surface defects are desired to achieve a more uniform corrosion mode and lower corrosion rate than those with high degrees of structural disorder and compositional fluctuations [33–35].

These previous work indicate the contradictory effects of chemical heterogeneity on the mechanical and corrosion properties of MGs. While most studies have evaluated these two properties separately, few work has been performed to simultaneously evaluate its effects on TFMGs during simultaneous mechanical and chemical loads. In this work, the effects of nanoscale chemical heterogeneity on the wear, corrosion, and tribocorrosion properties of ZrCuNiAl TFMGs were investigated by examining two types of samples: heterogeneous and homogeneous Zr-TFMGs. The former exhibit domains with compositional fluctuations of  $\sim 1.1\%$  Zr and  $\sim 0.5\%$  Cu, separated at  $\sim$ 413.0  $\pm$  64.7 nm. On the other hand, the homo-Zr samples exhibited chemical homogeneity even at the nanoscale (to the resolution limit of scanning electron based energy dispersive X-ray spectroscopy). The goals of the present study include: 1) quantification of the wear, corrosion, and tribocorrosion resistance of Zr-based TFMGs, 2) evaluation of the effects of chemical heterogeneity on mechanical properties and the passive film property, and 3) understanding the effects of chemical heterogeneity on the depassivation and repassivation kinetics of Zrbased TFMGs during tribocorrosion in 0.6 M NaCl solution.

#### 2. Experimental methods

#### 2.1. Materials synthesis

A base pressure of  $7 \times 10^{-5}$  Pa was achieved prior to film depositions. Zr<sub>51</sub>Cu<sub>34</sub>Ni<sub>8</sub>Al<sub>7</sub> films of ~200 nm thickness were deposited on Si substrates using radio frequency (RF) magnetron sputtering at RF power of 100 W, deposition time of 30 min, working distance of 10 cm, direct-current substrate bias of 50 V, and substrate rotation of 20 rpm without intentional substrate heating. The target is a quaternary Zrbased alloy with a composition similar to that of the film. Two sets of Zr-TFMG samples were prepared, with heterogeneous (hereafter referred as heter-Zr) and homogeneous (hereafter referred as homo-Zr) chemical distribution, by adjusting Ar pressure to be around 5 mTorr ( $\sim$ 6.7  $\times$  10<sup>-1</sup> Pa) and 3 mTorr ( $\sim$ 4  $\times$  10<sup>-1</sup> Pa) respectively, while Ar flow rate was kept constant at 20 sccm. These samples were then used for scratch, corrosion, and tribocorrosion tests later on. It is believed that such different Ar pressure leads to variations in the chemical heterogeneity of the deposits [36,37]. A more detailed description of the synthesis procedure can be found in [13,38].

#### 2.2. Characterization of mechanical properties

The mechanical properties of the samples were measured by nanoindentation tests (Hysitron Ti900) using a standard diamond Berkovich indenter following the Oliver and Pharr method [39]. Prior to indentation, the tip-area function was calibrated using a fused quartz sample. A trapezoidal loading function was applied, with 5 s loading/unloading time and 2 s holding time at 2–3 mN. Special care was taken during the indentation to minimize the substrate effect by ensuring that the maximum indentation depth was less than  $\sim$ 20% of the total film thickness [40]. The reported results represent average values obtained from more than ten repeated tests for each sample sets.

# 2.3. Electrochemical measurement

Potentiodynamic polarization (PD) tests were conducted in a typical three electrode configuration at ambient temperature in naturally aerated 0.6 M NaCl aqueous solution (pH  $\sim$  6.4  $\pm$  0.3) using a Gamry Reference 600® potentiostat. The as-deposited samples, mixed metal oxide coated titanium mesh, and a commercial silver-silver chloride electrode (1 M KCl internal solution) served as the working (WE), counter (CE), and reference electrode (RE) respectively. An exposed area of  $\sim 1 \times 1.5 \text{ cm}^2$  was prepared on the samples using a protective stop-off lacquer. PD tests were conducted after 1 h of immersion of the sample in the electrolyte for stabilizing the open circuit potential (OCP). The scan was performed at a rate of 0.167 mV/s, starting at a potential ~200 mV cathodic to OCP and terminated when a rapid increase in the anodic current density took place, reaching 1 mA/cm<sup>2</sup>. Tafel extrapolation was performed by selecting a linear portion of the PD curve approximately 100 mV above and below the corrosion potentials (Ecorr) to determine the corrosion current densities (icorr) of both samples. To examine the behavior of the passive film, Mott-Schottky (MS) analysis were conducted for five days. MS tests were conducted from 0 to 300 mV vs. OCP in the anodic region at 1 kHz frequency, 10 mV rms amplitude, and 10 mV/s potential sweeping rate.

### 2.4. Dry scratch and tribocorrosion tests

Dry scratch tests of both samples were conducted using a multifunctional tribometer (Rtec Instruments, CA, USA). Dry scratch tests were performed under 0.2 N normal load, 0.2 mm/s sliding velocity, over 5 mm total scratch length for 25 s in air. A diamond tip (12.5  $\mu m$  radius) was used as the counter body, and the contact between the tip and sample was maintained for 5 s before each test.

Tribocorrosion tests were performed under 0.2 N normal load,

0.2 mm/s sliding velocity, over 5 mm total scratch length for 25 s against diamond tip (12.5 µm radius) counter body. During the tribocorrosion test, a three-electrode setup was used, where the as-deposited sample (with  $\sim 1 \times 1.5 \text{ cm}^2$  exposed area), activated titanium mesh, and 1 M KCl Ag/AgCl electrode were used as the WE, CE, and RE, respectively, immersed in 0.6 M NaCl aqueous solution. This setup was connected to a potentiostat/galvanostat/zero resistance ammeter (Gamry Reference 600™ system). The electrolyte used was  $\sim 40 \text{ ml}$  of 0.6 M NaCl aqueous solution, open to air. During the tribocorrosion test, both of samples were tested under two different applied potential conditions: an anodic potential of 400 mV above OCP (OCP + 0.4 V) and OCP. Before each test, the current/potential was stabilized for  $\sim 10$ –20 min. Unless specified otherwise, all results reported here were averaged from at least three repeated tests.

#### 2.5. Materials characterization

The composition and morphology of sample surfaces and cleaved cross-sections were characterized by a field-emission scanning electron microscopy (FESEM, LEO 1550) with an Oxford INCASynergy energy dispersive X-ray spectroscopy (EDS). To reveal any compositional heterogeneity, the as-deposited samples were etched in 1 ml HNO3: 5 ml  $C_2H_6O$  solution for 30 s at room temperature. A grazing incidence X-ray diffractometer (GIXRD, Panalytical X'pert) with a wavelength of 1.54 Å Cu K $\alpha$  under 45 kV and 40 mA were used to characterize the microstructure of as-deposited thin film samples. After dry scratch and tribocorrosion tests, the cross-sections of wear tracks were studied using focus ion beam microscopy (FIB, Helios600) at 30 kV and 0.9 nA current. A protective Pt layer ( $\sim\!0.3-1.5~\mu m$ ) was deposited on the sample surfaces prior to milling of the cross-sectional samples.

#### 3. Results and discussion

## 3.1. Characterization of as-deposited Zr-TFMGs

Fig. 1 presents the GIXRD patterns of the as-deposited thin films, where the typical broad hump diffraction peaks were observed at 20 angle of  $\sim 36^{\circ}$ , confirming the amorphous nature of both samples, similar to prior report [41]. Fig. 2(a) and (b) show the surface morphology of the as-deposited heter-Zr and homo-Zr samples. Both samples exhibited a mirror finish to the naked eye and are featureless under SEM. After etching process, the homo-Zr sample remains featureless, as shown in Fig. 2(d). However, networks of deep etched grooves were observed in heter-Zr sample (indicated by arrow in Fig. 2(c)),

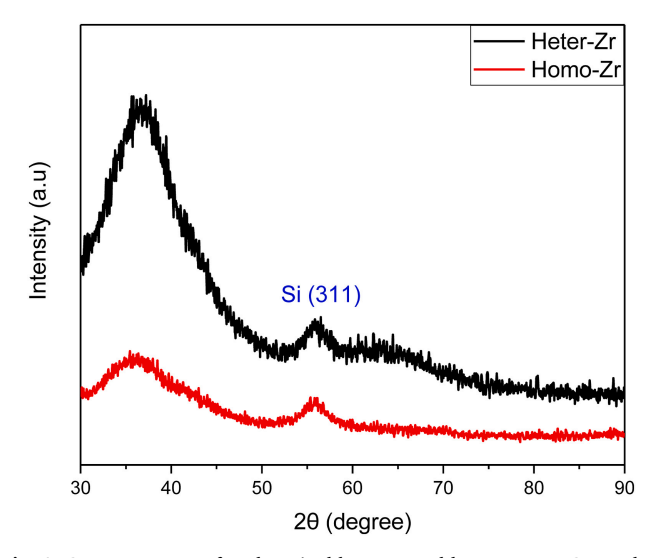


Fig. 1. GIXRD patterns of as-deposited heter-Zr and homo-Zr TFMG samples.

suggesting the presence of nanoscale chemical heterogeneity within and outside the groove region that result in different etching rates on the surface. EDS analysis of heter-Zr reveal a compositional fluctuation of 1.1 at.% Zr and 0.5 at.% Cu within and outside the groove region, as summarized in Table 1. A similar but more dramatic chemical heterogeneity has been reported in  $\text{Cu}_{47.5}\text{Zr}_{47.5}\text{Al}_5$  MG [42] where two amorphous phases were formed by liquid phase separation, with compositional differences of  $\sim$ 8.5 at.% Cu, 12.9 at.% Zr and 4.4 at.% Al.

To evaluate whether such mild chemical heterogeneity would affect the mechanical properties of TFMGs, both samples were cleaved via clippers with the thin film on the tensile side. Fig. 2(e) and (f) show the fractography of both samples. It can be seen that while homo-Zr exhibited clearly brittle fracture with a smooth fractured surface, heter-Zr exhibited a more corrugated fractured surface, indicating its better fracture resistance and potentially higher ductility. These results confirm the high sensitivity of both chemical and mechanical properties of Zr-TFMG due to variations of processing conditions (i.e. Ar working pressure).

The microstructure of thin films deposited by PVD is often found to be dominated by growth instabilities originating from a competition between surface diffusion and self shadowing, which can be tailored by controlling various deposition parameters such as deposition angle, substrate rotation, and the working pressures of Ar [36,37,43]. For example, Denis et al. [43] studied the effects of different working pressures of Ar from 0.4 to 10 Pa, and observed a thin film growth mode transition in Au-based thin film metallic glasses. As reported in previous research [44], under higher Ar working pressure, the probability of ion collisions between Ar and deposited elements is increased, resulting in more cluster growth. Under low Ar working pressure, the kinetic energy of atoms will be well reserved to overcome the shadowing effect (i.e. adatoms transferring from surface peaks to valleys), causing the formation of more homogeneous microstructure [43,45]. In addition, high working pressure can minimize the preferential ejection effect during sputtering owing to the diverse mass of the sputtering elements, resulting in slightly higher Zr concentration in the heter-Zr sample [44].

# 3.2. Nanomechanical properties

The hardness and elastic modulus of both samples were obtained after a series of nanoindentation tests under 2-3 mN normal load. These normal loads were chosen to maximize the indentation depth (to avoid indentation size effect) [46,47] yet minimize the substrate effect based on the thin film thickness. The typical indentation depths of both samples were around 30 nm. Fig. 3 and Table 3 summarize the mechanical properties of both sample sets. Both hardness (H) and elastic modulus (E) values obtained are comparable to those reported before for similar Zr-based TFMGs or BMGs [48,49]. It can be also seen that the heter-Zr samples exhibit lower H and higher E values than those of homo-Zr samples. The contradictive mechanical properties (i.e. higher elastic modulus but lower hardness) of heter-Zr could not be explained using a simple rule of mixture (ROM) of modulus and hardness [50]. The difference in modulus could be related to the different relaxation state of the glassy films, consistent with prior report [51]. Upon deposition, the heter-Zr samples produced by higher Ar working pressure (lower kinetic energy of deposition) possess a longer time for the deposited atoms to relax, reaching a lower energy state that gives rise to a higher modulus. The homo-Zr samples, on the other hand, involve relatively fast surface diffusion of the deposited atoms, retaining a higher energy state and thus a lower modulus. In addition, the smaller average interatomic distance (d/K) in heter-Zr could also contribute to its higher modulus than homo-Zr [52]. According to the diatomic gas model [53], the average interatomic distance (d/K) can be measured from XRD results following  $K\lambda = 2dSin\theta_m$ , where  $\lambda$  is the wavelength Cu- $K\alpha$  $(0.154 \text{ nm}), \theta_{\text{m}}$  is the angle of the broad peak, d is the atomic spacing of a diatomic gas, and K is assumed to be an unknown constant for an amorphous solid (K = 1.23 for a diatomic gas). The average

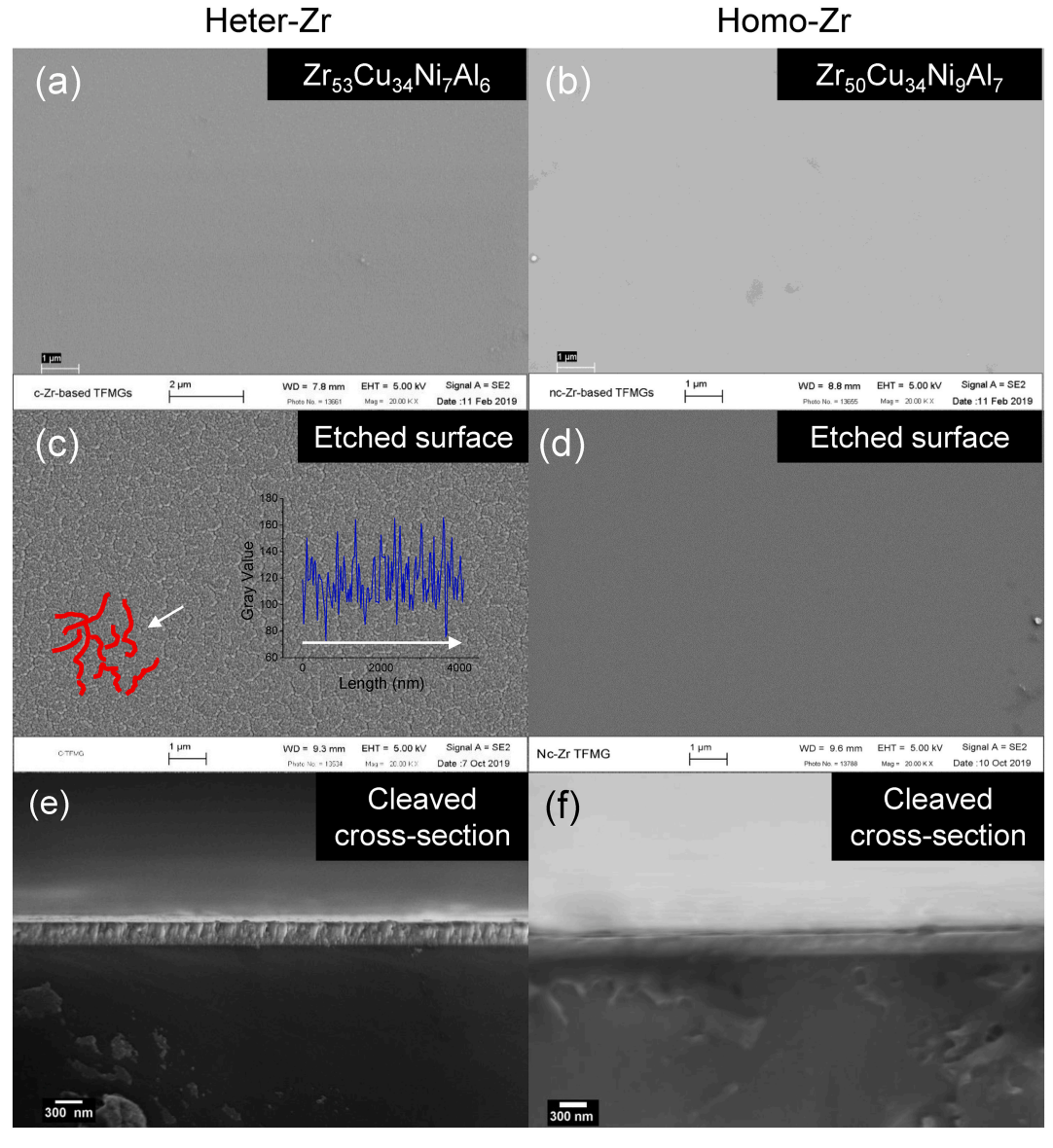


Fig. 2. SEM images of (a, b) as-deposited surface (c, d) etched surface and (e, f) cross section after cleaving of heter-Zr and homo-Zr TFMG samples. Inset line profile in (c) shows the greyscale profile measured along the horizontal white arrow direction.

Table 1
Summary of global and local compositions of heter-Zr and homo-Zr samples from EDS analysis. The boundary areas of heter-Zr are marked by red lines in Fig. 2(c) while areas away from these boundaries are referred as interior.

Sample ID	Zr (at. %)	Cu (at. %)	Ni (at. %)	Al (at. %)
Homo-Zr (global) Heter-Zr (global) Heter-Zr (Interior) Heter-Zr (boundary)	52.6 ± 0.54 51.7 ± 0.68	33.8 ± 0.68 33.9 ± 0.35 34.0 ± 0.42 33.5 ± 0.17	$7.4 \pm 0.04$ $7.7 \pm 0.23$	$6.1 \pm 0.69$ $6.5 \pm 0.12$

interatomic distance of heter-Zr (d/K  $\sim$  0.244) is smaller than that of homo-Zr (d/K  $\sim$  0.247), indicating denser atomic packing state as well as to stronger atomic interaction in heter-Zr.

On the other hand, the difference in hardness speaks to the importance of nanoscale chemical variation induced by processing. Such observations are in qualitative agreement with prior experimental and simulation work of Wang et al. [29,54]. Notably, for spatially homogenous MG samples the plastic deformation is controlled by stress-driven nucleation of a catastrophic shear band, which requires higher

stress and leads to brittle failure, consistent with our results of homo-Zr. As the spatial heterogeneity increases, the deformation mechanism transforms to strain percolation of multiple shear bands from local soft regions, resulting in a decrease in strength (or hardness) and an increase in ductility, similar to those seen in heter-Zr films. Furthermore, the different elastic modulus mismatch between the thin film and substrate could be another factor for the different ductility of the two samples [48]. The elastic modulus of standard Si is 187  $\pm$  8 GPa, exhibiting a lower elastic modulus mismatch with heter-Zr ( $E_{\rm heter-Zr}=145.8~\pm~7.36$  GPa) than with homo-Zr ( $E_{\rm homo-Zr}=100.8~\pm~1.8$  GPa). More compatible elastic modulus between the thin film and the substrate can reduce the interfacial stress discontinuities and minimize brittle failure [55].

Based on the mechanical differences, heter-Zr and homo-Zr samples are expected to lead to different tribological behavior. While bulk materials' wear rate is typically inversely related to their surface hardness according to the classical Archard's law [56], for thin film materials, it has been reported that the ratio between hardness and elastic modulus (H/E) serves as a better indicator for wear resistance. Typically a higher H/E ratio is associated with better wear resistance

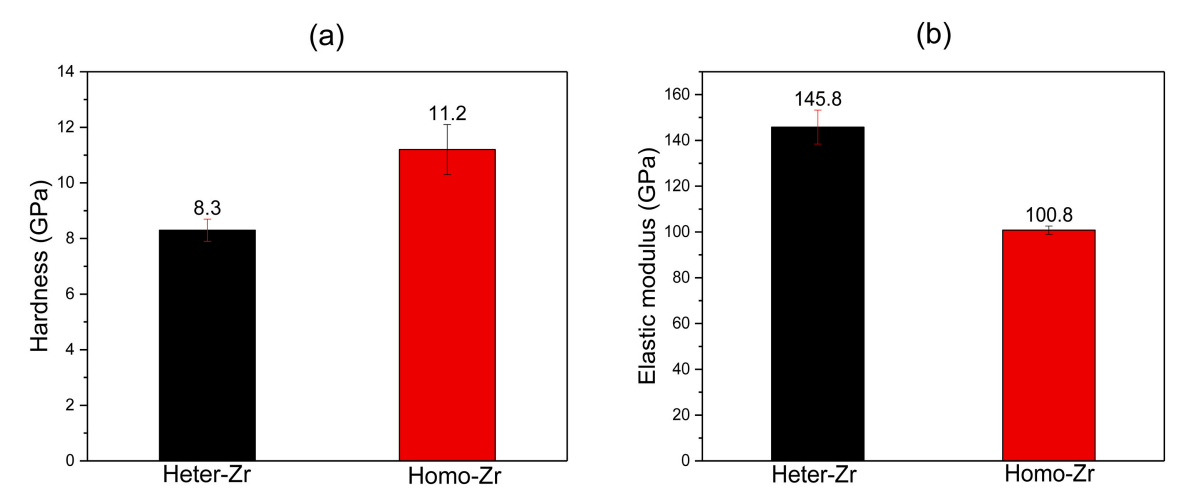


Fig. 3. Summary of (a) hardness and (b) elastic modulus of heter-Zr and homo-Zr TFMGs measured from nanoindentation tests.

[48]. It can be seen from Table 3 that the H/E value of the homo-Zr sample (0.1) is higher than that of heter-Zr sample (0.06), suggesting a better wear resistance of the former. As shown in the next section, such a prediction is in agreement with the dry scratch test results.

#### 3.3. Corrosion behavior

Fig. 4(a) shows the typical PD curves of both samples tested in 0.6 M NaCl solution. Table 2 summarizes all measured electrochemical parameters from the PD tests. The polarization resistance ( $R_p$ ) was calculated by the Stern-Gray equation as [57].

$$i_{corr} = \frac{\beta_a \beta_c}{2.3 \times R_p (\beta_a + \beta_c)}, \tag{1}$$

where  $\beta_a$  and  $\beta_c$  are the slopes of the anodic and cathode curve respectively. It can be seen that while both samples exhibit similar OCP,  $i_{corr}$  of homo-Zr is slightly lower than that of heter-Zr. The homo-Zr sample exhibited a pitting potential of  $\sim 1.05$  V vs. Ag/AgCl, while heter-Zr showed no apparent sudden increase of corrosion current as those seen at pitting potential of homo-Zr in the whole scan range. Such results suggest that the heter-Zr samples exhibit a higher pitting resistance than its homo-Zr counterpart in 0.6 M NaCl aqueous solution albeit its slightly lower  $i_{corr}$ . Visual inspections (results not shown here) of both samples after tribocorrosion at anodic potential from the next section further confirms the higher pitting tendency of homo-Zr than heter-Zr. Such observation contradicts the common belief that chemical heterogeneity imposes detrimental effects on corrosion resistance [58],

but is in agreement with several prior research that indicates corrosion resistance of MGs containing passive elements increase after structural relaxation [31,59,60] due to the releasing of internal stress [31] and reduction of free volume in the as-prepared amorphous alloy [59]. Indeed, there is growing evidence to indicate that mild nanoscale chemical heterogeneity, introduced either during processing or low temperature annealing, behaves rather differently from their micron-sized counterparts in affecting corrosion resistance [61-63]. For example, Asami et al. [61] found that the corrosion resistance of amorphous Cr-Zr alloys was improved via nano precipitation when the size of Zr precipitates is less than 20 nm. An increased Cr concentration was found in the passive film to enhance its protectiveness over the whole surface. Interestingly, a similar critical size of ~20 nm (of Al-rich precipitate) was also identified in amorphous Al-Cr system [63], above which the corrosion resistance decreases. In this work, we assume that the higher resistance of heter-Zr to pitting initiation and growth is attributed to the uneven distribution of elements and the Zr-enriched boundary structure (i.e. marked by the red lines in Fig. 2(c)) [62]. Under neutral pH, according to the thermodynamic calculations of dissolved ions vs. oxide stability (i.e. the Pourbaix diagram), the passive layers of both alloys are assumed to contain primarily ZrO<sub>2</sub> and Al<sub>2</sub>O<sub>3</sub>. Since Al content is small in the alloy, and remains close to  $\sim$ 6.5–6.9 at. % in both homo-Zr, its effects on the different corrosion behavior is negelected here. The slight enrichment of Zr in the boundaries of heter-Zr (~2.5 at.% higher than that of homo-Zr) could promote the formation of a more compact ZrO2 structure on the surface. Such 'network' of Zr-rich boundaries may act similarly (probably to a much less extent) as

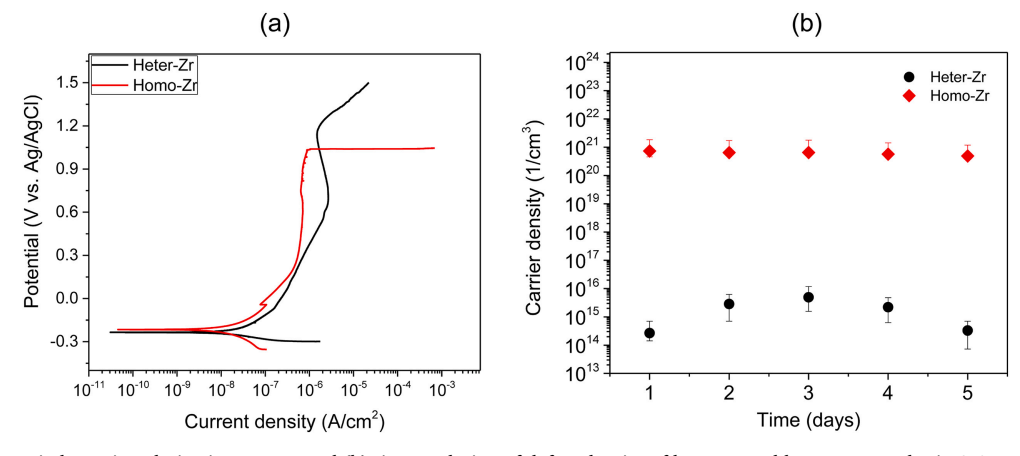


Fig. 4. (a) Typical potentiodynamic polarization curves, and (b) time evolution of defect density of heter-Zr and homo-Zr samples in 0.6 M NaCl aqueous solution. Error bars in (b) represent one standard deviation from all repeated tests.

Table 2 Summary of electrochemical parameters from PD tests of homo-Zr and heter-Zr sampels in 0.6 M NaCl.

Sample ID	E <sub>corr</sub> (mV)	E <sub>pit</sub> (mV)	$E_{pit}$ - $E_{corr}$ (mV)	i <sub>corr</sub> (nA/cm²)	$\beta_a$ (V/decade)	$\beta_c$ (V/decade)	$R_p$ (x $10^6 \Omega \text{ cm}^2$ )
Homo	-204.3	0.98	205.3	20.98	0.61	0.59	2.17
-Zr	± 11.2	$\pm 0.1$	± 11.2	± 25.6	± 0.47	± 0.46	± 0.43
Heter	-202.7	NA	NA	23.69	0.24	0.08	1.68
-Zr	± 45.5			± 12.5	± 0.03	± 0.01	± 1.43

grain boundaries in crystalline passive alloys. For crystalline passive alloys, it is thought that smaller grain size, hence higher grain boundary density influences corrosion resistance by affecting the rate of ion transport through the passive film, as well as the passive film dissolution rate [64]. For nanocrystalline materials that have a much higher grain boundary density at the surface compared to their microcrystalline counterparts, these boundaries lead to higher average surface reactivity through increased electron state density and diffusional defect transport.

To further quantify the differences in the passive film property, MS analysis was conducted for five days for homo-Zr and heter-Zr samples, as shown in Fig. 4(b). The charge carrier density was calculated as [65]:

$$\frac{1}{C^2} = \frac{\pm 2}{\varepsilon \varepsilon_0 eN} \left( E - E_{fb} - \frac{kT}{q} \right), \tag{2}$$

where C is the capacitance,  $\epsilon$  is the passive film dielectric constant,  $\epsilon_0$  is the permittivity of vacuum (8.85  $\times$  10<sup>-14</sup> F/cm), N is the charge carrier concentration, E is the applied potential,  $E_{fb}$  is the flat band potential, k is the Boltzmann constant (1.38  $\times$  10<sup>-23</sup> JK<sup>-1</sup>), T is the absolute temperature and q is the elementary charge (1.602  $\times$  10<sup>-19</sup>C). It can be seen that the heter-Zr samples contain  $\sim$  fiver orders of magnitude lower defect density than homo-Zr. Since the defect density in the passive film is proportional to the sample's pitting susceptibility, a much higher pitting resistance is expected in heter-Zr.

#### 3.4. Dry scratch test

The surface morphologies of both samples after dry scratch test are shown in Fig. 5(a) and (b). Worn surfaces of both samples are quite smooth. On the worn surface of heter-Zr samples, pile-ups could be seen at the edges of the wear track, indicating extensive plastic deformation during abrasive wear [66]. On the other hand, no visible pile-up could be seen on homo-Zr samples. Instead, loose wear debris was frequently observed along the side of the wear track, indicating a lack of plastic deformation and more brittle failure on the surface, consistent with its higher hardness and lower compliance (lower E), and more brittle fracture than its heter-Zr counterparts. Cross-sectional SEM images (not shown) reveal that the heter-Zr sample exhibits a deeper and slightly

narrower wear track than homo-Zr sample, ultimately resulting in higher material volume loss than homo-Zr sample, as summarized in Fig. 8, in agreement with the H/E ratio prediction [48]. The coefficient of friction (COF) of both samples is shown in Fig. 5(c). It can be seen that the heter-Zr sample exhibits a higher average COF ( $\sim$ 0.46) than that of homo-Zr sample ( $\sim$ 0.37) during dry scratch test, consistent with its higher wear rate [14].

#### 3.5. Tribocorrosion behavior

Fig. 6(a) shows the evolution of current during the tribocorrosion tests of both samples. The dashed lines mark the start and finish of the scratch test. It can be seen that the overall current density of both samples are much higher under the anodic potential (0.4 V above OCP) than that under OCP. Under the anodic potential, the current remained almost constant before the indenter probed the surface, and shifted to more positive values during scratching, indicating positive wear-corrosion synergy (i.e. wear accelerate corrosion). Such positive shift of current is likely due to the depassivation on the wear track, where the surface passive film is locally destroyed or removed, exposing the more active, and unprotected thin film material. Once the test was finished, the current of both samples recovered their original state, indicating repassivation on the wear track. It is noted that the current evolution of homo-Zr under the anodic potential shows an abrupt increase before the initiation of the scratch test due to early film dissolution (indicated by arrow in Fig. 6(a)). In addition, film delamination was observed by visual inspection at the end of the test, hence their results are not included in Fig. 6(b) and Fig. 7 later on. Overall, the much higher corrosion current rise during scratch as well as early film dissolution of homo-Zr indicates its poorer tribocorrosion resistance than that of heter-Zr under the testing condition.

During the tribocorrosion test, COF of both samples was much lower than that of the dry scratch test, as shown in Fig. 6(b), probably due to the lubrication effects of the electrolyte [67]. COF of homo-Zr under the anodic potential is not presented here due to film delamination during tribocorrosion. Interestingly, the average COF values of heter-Zr sample ( $\sim$ 0.08 under OCP + 0.4 V and  $\sim$ 0.05 under OCP) is lower than that of homo-Zr sample ( $\sim$ 0.13), suggesting that its passive film is more effective in reducing friction. This is rather surprising as ZrO<sub>2</sub> has very

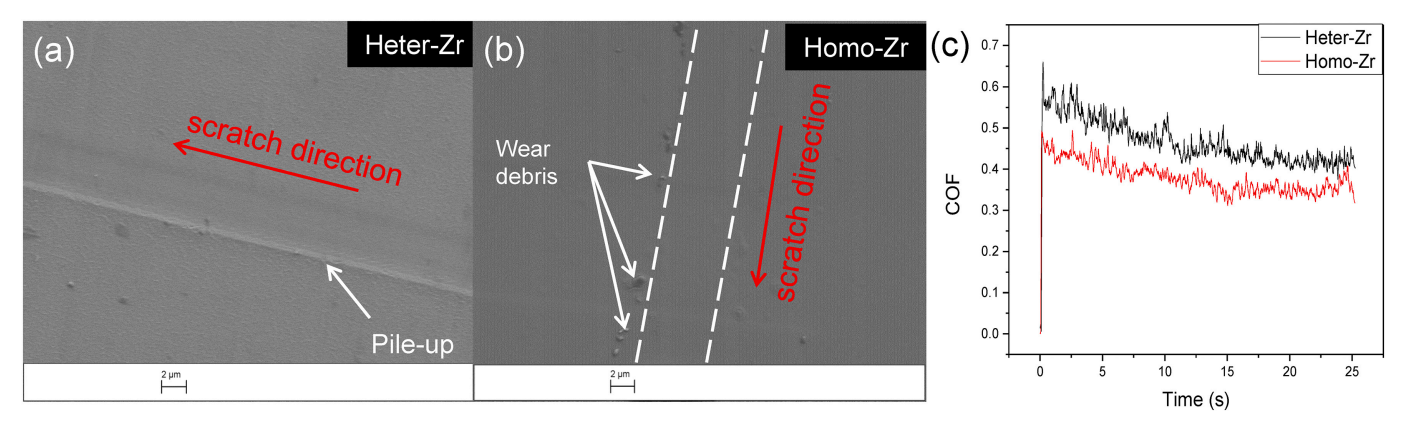


Fig. 5. (a, b) Surface SEM images and (c) COF of heter-Zr and homo-Zr samples after dry scratch test. Dashed lines in (b) indicate the edges of the wear track.

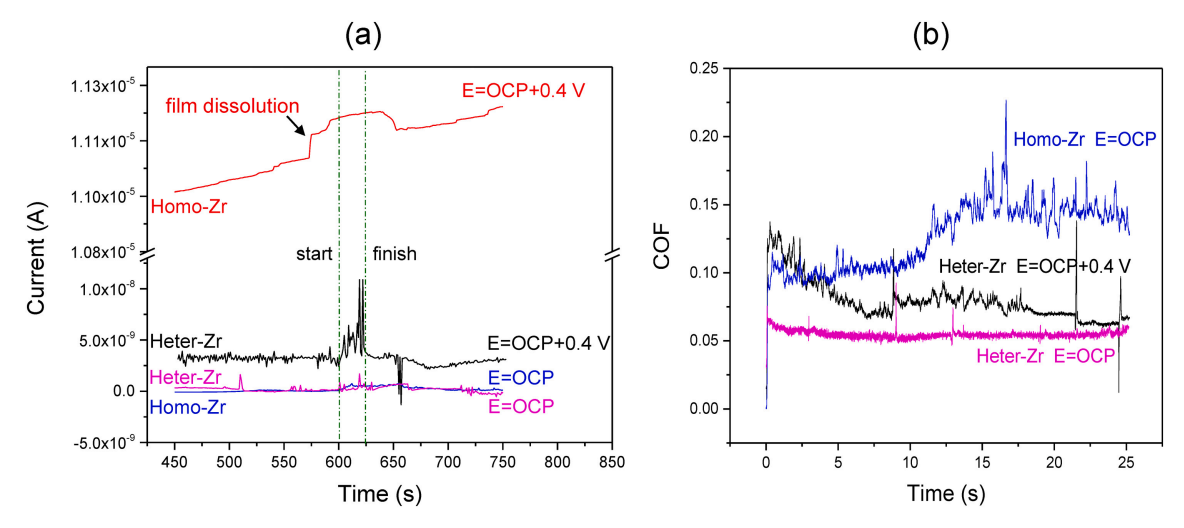


Fig. 6. (a) Current evolution and (b) coefficient of friction (COF) of heter-Zr and homo-Zr samples during tribocorrosion under OCP and anodic applied potential (400 mV above OCP). Dashed lines in (a) mark the start and finish of the scratch by the counterbody.

low ionic potential and is generally associated with higher friction (i.e. abrasive rather than lubricious) [68]. More work is required to quantify the composition, structure, and properties of these passive films, which is left for future work.

Fig. 7 shows the surface SEM images of both samples after the tribocorrosion tests. The worn surfaces of heter-Zr and homo-Zr samples under OCP condition, as shown in Fig. 7(a) and (b), are similar to that observed under dry scratch test. Cross-sectional SEM images in Fig. 7(d-f) show that there is very little material loss for both samples and no film delamination. Table 3 summarizes the wear track dimensions and the calculated material volume loss. Under OCP, a narrower and shallower wear track was observed in heter-Zr, resulting in a tribocorrosion rate ~38% lower in heter-Zr sample than homo-Zr sample, as shown in Fig. 8. Under the anodic potential (0.4 V above OCP), the wear track of heter-Zr sample (Fig. 7(c)) appears to be deeper than that under OCP, with extensive shear bands formation, typical for MGs after plastic

deformation [28,49,50]. EDS analysis (Fig. 7(a-c) insets) reveals that all elements including oxygen are uniformly distributed on the worn surfaces. A much higher oxygen concentration was observed on the wear track of heter-Zr under the anodic potential than under OCP. In addition to the higher oxidation driving force at the anodic potential, it is likely that the presence of extensive shear bands with excess free volume also promotes the surface chemical reactivity with oxygen [59].

To further quantify chemical wear during tribocorrosion under the anodic potential, the amount of material loss due to corrosion was calculated for both samples using Faraday's law as  $V_{chem} = QM/nF\rho$ , where Q is the total charge transferred from the start to finish during tribocorrosion test at E=0.4~V above OCP, M is the atomic mass ( $\approx 73.77~g/mol$ ), n is the valence ( $\approx 1.81$ ), F is the Faraday's constant (96,500C/mol), and  $\rho$  is the density ( $\approx 7.13~g/cm^3$ ) of Zr-based TFMG [69]. Fig. 8 shows the chemical wear ( $V_{chem}$ ) of heter-Zr sample is around  $4.62\times 10^{-9}~mm^3$ , which is about two orders of magnitude

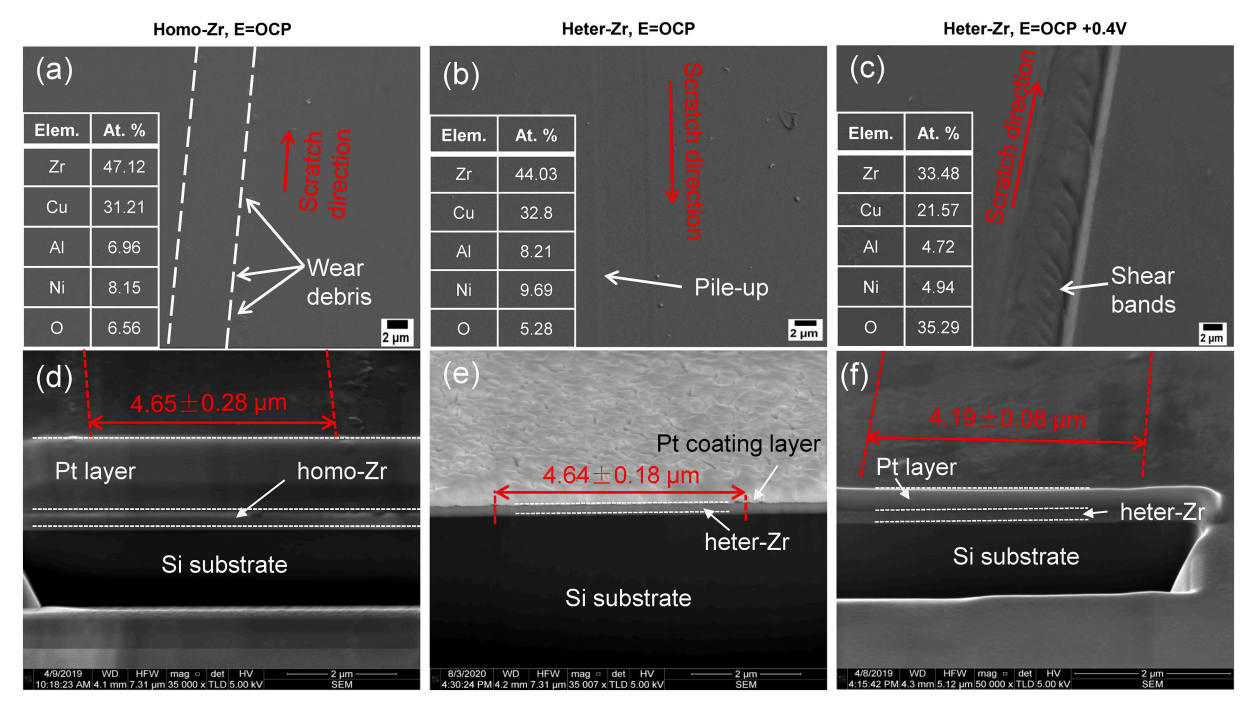
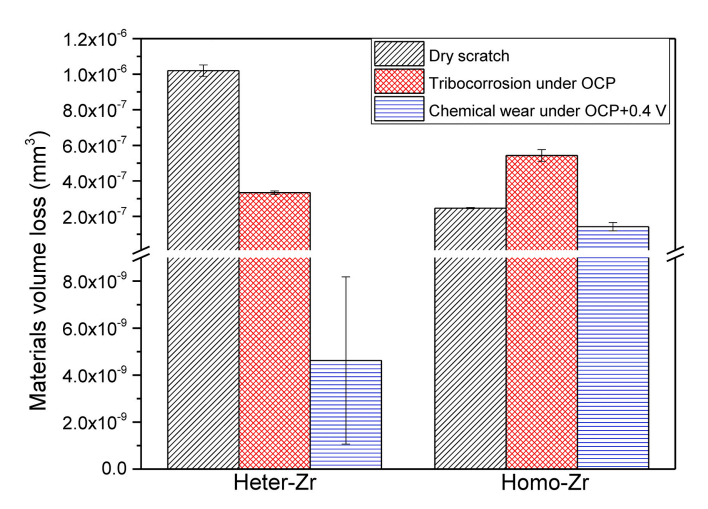


Fig. 7. (a-c) Surface and (d-f) cross-sectional SEM images of homo-Zr and heter-Zr samples after tribocorrosion test (OCP for homo-Zr; OCP and OCP  $\pm$  0.4 V anodic applied potential for heter-Zr). Dashed lines in (a, d-f) indicate the edges of the wear track. Insets in (a-c) show the element compositions (at. %) obtained by EDS analysis on the wear tracks.

Table 3
Summary of mechanical properties, dry scratch, and tribocorrosion test results of heter-Zr and homo-Zr samples. H and E represent hardness and elastic modulus respectively, obtained from nanoindentation tests. d, w, and V represents the wear track depth, width, and total material loss in volume respectively, measured after dry scratch and tribocorrosion tests.

Sample ID	H (GPa)	E (GPa)	H/E	Dry Scratch			Tribocorrosion			
		(Gra)		d (x10 <sup>-5</sup> mm)	w (x10 <sup>-3</sup> mm)	V (x10 <sup>-7</sup> mm <sup>3</sup> )	d (x10 <sup>-5</sup> mm)	w (x10 <sup>-3</sup> mm)	V (x10 <sup>-7</sup> mm <sup>3</sup> )	Corrosion potential
Heter-Zr	8.3 ± 0.4	145.8 ± 7.4	0.06	5.7 ± 1.4	3.59 ± 0.1	$10.2 ~\pm~ 0.3$	2.7 ± 1.1 1.4 ± 0.7	4.19 ± 0.08 4.64 ± 0.18	$5.66 \pm 0.12$ $3.34 \pm 0.1$	OCP + 0.4 V OCP
Homo-Zr	11.2 ± 0.9	100.8 ± 1.8	0.1	1.4 ± 0.6	$3.66 \pm 0.5$	$2.47 \pm 0.03$	$2.3~\pm~0.8$	$4.65 \pm 0.28$	$5.43 \pm 0.33$	OCP



**Fig. 8.** Summary of material volume loss of heter-Zr and homo-Zr samples after dry scratch and tribocorrosion tests under OCP and anodic potentials. Error bar represents one standard deviation from all repeated tests.

lower than that of homo-Zr sample ( $V_{\rm chem}=1.43\times10^{-7}~{\rm mm}^3$ ). The chemical wear during tribocorrosion was dominated by their respective corrosion properties, where homo-Zr exhibited higher material loss than heter-Zr, in consistent with their pure corrosion behavior. Overall, the results in this section showed that nanoscale chemical heterogeneity affects both the mechanical and electrochemical properties of Zr-TFMGs, which act synergistically to result in a better tribocorrosion resistance in heter-Zr than homo-Zr sample under the selected testing conditions.

#### 4. Conclusions

In this work, the effects of chemical heterogeneity on the wear, corrosion, and tribocorrosion resistance of magnetron sputtered ZrCuNiAl TFMGs were evaluated by comparing two sets of sample: heter-Zr and homo-Zr. The presence of nanoscale (~ 413 nm) chemical heterogeneity ( $\sim 1.1\%$  Zr and 0.5% Cu) was found to significantly affect the mechanical properties, resulting in lower hardness and higher ductility in heter-Zr than homo-Zr. As a result, the dry scratch wear resistance of homo-Zr was higher than that of heter-Zr samples. On the other hand, such nanoscale chemical heterogeneity affects the pitting corrosion in the opposite trend, where heter-Zr was found to outperform homo-Zr. Mott-Schottky analysis showed that the presence of nanoscale chemical fluctuations of Zr and Cu at the surface promoted the formation of a more protective passive film with lower defect density during corrosion. Finally, the tribocorrosion resistance of heter-Zr samples was found to be better than that of homo-Zr sample while the chemical wear was dominated by their respective electrochemical properties. The results of the present work may shed light on future structural optimization strategies for improving reliability of TFMGs under combined surface stress and corrosion conditions.

#### CRediT authorship contribution statement

Wenbo Wang: Investigation, Validation, Writing - original draft. Hesham Mraied: Investigation. Wahyu Diyatmika: Investigation, Writing - original draft. Jinn P. Chu: Supervision, Writing - original draft. Lin Li: Writing - original draft. Wenjun Cai: Conceptualization, Supervision, Writing - review & editing.

#### **Declaration of competing interest**

The authors declare that they have no known competing financial interests or personal relationships that could have appeared to influence the work reported in this paper.

#### Acknowledgments

This work was partially supported by the Applied Research Center for Thin-Film Metallic Glass from The Featured Areas Research Center Program within the framework of the Higher Education Sprout Project by the Ministry of Education (MOE) in Taiwan. WW, HM and WC gratefully acknowledge the financial support by the US National Science Foundation under Grant DMR-1856196 and CMMI-185651. W.W. sincerely acknowledge Ya-peng Yu and Stephen McCartney at Virginia Tech for their assistance in sample preparation FIB analysis. LL acknowledge the financial support by the US National Science Foundation under CMMI- 170267.

#### References

- L. Tian, Y.Q. Cheng, Z.W. Shan, J. Li, C.C. Wang, X.D. Han, J. Sun, E. Ma, Approaching the ideal elastic limit of metallic glasses, Nat. Commun. 3 (2012).
- [2] H. Ma, J. Xu, E. Ma, Mg-based bulk metallic glass composites with plasticity and high strength, Appl. Phys. Lett. 83 (14) (2003) 2793–2795.
- [3] J. Eckert, J. Das, K.B. Kim, F. Baier, M.B. Tang, W.H. Wang, Z.F. Zhang, High strength ductile Cu-base metallic glass, Intermetallics 14 (8) (2006) 876–881.
- [4] D.R. Maddala, A. Mubarok, R.J. Hebert, Sliding wear behavior of Cu50Hf41.5Al8.5 bulk metallic glass, Wear 269 (7) (2010) 572–580.
- [5] R. Salehan, H.R. Shahverdi, R. Miresmaeili, Effects of annealing on the tribological behavior of Zr60Cu10Al15Ni15 bulk metallic glass, J. Non-Cryst. Solids 517 (2019) 127–136.
- [6] M. Gao, W. Lu, B. Yang, S. Zhang, J. Wang, High corrosion and wear resistance of Al-based amorphous metallic coating synthesized by HVAF spraying, J. Alloys Compd. 735 (2018) 1363–1373.
- [7] G. Perumal, H.S. Grewal, A. Ayyagari, S. Mukherjee, H.S. Arora, Enhancement in bio-corrosion resistance of metallic glass by severe surface deformation, Appl. Surf. Sci. 487 (2019) 1096–1103.
- [8] T.C. Hufnagel, C.A. Schuh, M.L. Falk, Deformation of metallic glasses: recent developments in theory, simulations, and experiments, Acta Mater. 109 (2016) 375–393.
- [9] J.J. Kruzic, Bulk metallic glasses as structural materials: a review, Adv. Eng. Mater. 18 (8) (2016) 1308–1331.
- [10] A. Inoue, N. Nishiyama, New bulk metallic glasses for applications as magnetic-sensing, chemical, and structural materials, MRS Bull. 32 (8) (2007) 651–658.
- [11] M.F. Ashby, A.L. Greer, Metallic glasses as structural materials, Scr. Mater. 54 (3) (2006) 321–326.
- [12] S.X. Song, H. Bei, J. Wadsworth, T.G. Nieh, Flow serration in a Zr-based bulk metallic glass in compression at low strain rates, Intermetallics 16 (6) (2008) 813–818.
- [13] C.C. Yu, C.M. Lee, J.P. Chu, J.E. Greene, P.K. Liaw, Fracture-resistant thin-film metallic glass: ultra-high plasticity at room temperature, Apl Mater 4 (11) (2016).

- [14] J.P. Chu, J.S.C. Jang, J.C. Huang, H.S. Chou, Y. Yang, J.C. Ye, Y.C. Wang, J.W. Lee, F.X. Liu, P.K. Liaw, Y.C. Chen, C.M. Lee, C.L. Li, C. Rullyani, Thin film metallic glasses: unique properties and potential applications, Thin Solid Films 520 (16) (2012) 5097–5122.
- [15] J.P. Chu, T.Y. Liu, C.L. Li, C.H. Wang, J.S.C. Jang, M.J. Chen, S.H. Chang, W.C. Huang, Fabrication and characterizations of thin film metallic glasses: antibacterial property and durability study for medical application, Thin Solid Films 561 (2014) 102–107.
- [16] W. Diyatmika, J.P. Chu, B.T. Kacha, C.C. Yu, C.M. Lee, Thin film metallic glasses in optoelectronic, magnetic, and electronic applications: A recent update, Curr Opin Solid St M 19 (2) (2015) 95–106.
- [17] C.N. Cai, C. Zhang, Y.S. Sun, H.H. Huang, C. Yang, L. Liu, ZrCuFeAlAg thin film metallic glass for potential dental applications, Intermetallics 86 (2017) 80–87.
- [18] J.C. Ye, J.P. Chu, Y.C. Chen, Q. Wang, Y. Yang, Hardness, yield strength, and plastic flow in thin film metallic-glass, J. Appl. Phys. 112 (5) (2012).
- [19] M.H. Chuang, C. Wang, B.K. Chao, W.L. Kao, J.J. Shyue, C.H. Hsueh, Mechanical properties and microstructure of Zr-Ti-Ni thin film metallic glasses modified with minor SF6, Compos Part B-Eng 129 (2017) 243–250.
- [20] Y.L. Deng, J.W. Lee, B.S. Lou, J.G. Duh, J.P. Chu, J.S.C. Jang, The fabrication and property evaluation of Zr-Ti-B-Si thin film metallic glass materials, Surf. Coat. Technol. 259 (2014) 115–122.
- [21] Y. Wang, L.L. Shi, D.L. Duan, S. Li, J. Xu, Tribological properties of Zr61Ti2Cu25Al12 bulk metallic glass under simulated physiological conditions, Mat Sci Eng C-Mater 37 (2014) 292–304.
- [22] H.W. Jin, R. Ayer, J.Y. Koo, R. Raghavan, U. Ramamurty, Reciprocating wear mechanisms in a Zr-based bulk metallic glass, J. Mater. Res. 22 (2) (2007) 264–273.
- [23] P.H. Tsai, T.H. Li, K.T. Hsu, J.W. Chiou, J.S.C. Jang, J.P. Chu, Effect of coating thickness on the cutting sharpness and durability of Zr-based metallic glass thin film coated surgical blades, Thin Solid Films 618 (2016) 36–41.
- [24] P.J. Blau, Friction and wear of a Zr-based amorphous metal alloy under dry and lubricated conditions, Wear 250 (2001) 431–434.
- [25] X.Y. Fu, D.A. Rigney, M.L. Falk, Sliding and deformation of metallic glass: experiments and MD simulations, J. Non-Cryst. Solids 317 (1–2) (2003) 206–214.
- [26] E. Ma, J. Ding, Tailoring structural inhomogeneities in metallic glasses to enable tensile ductility at room temperature, Mater. Today 19 (10) (2016) 568–579.
- [27] J. Ding, S. Patinet, M.L. Falk, Y.Q. Cheng, E. Ma, Soft spots and their structural signature in a metallic glass, Proc. Natl. Acad. Sci. U. S. A. 111 (39) (2014) 14052–14056.
- [28] R. Rashidi, M. Malekan, R. Gholamipour, Microstructure and mechanical properties of a cu-Zr based bulk metallic glass containing atomic scale chemical heterogeneities, Mat Sci Eng a-Struct 729 (2018) 433–438.
- [29] N. Wang, J. Ding, F. Yan, M. Asta, R.O. Ritchie, L. Li, Spatial correlation of elastic heterogeneity tunes the deformation behavior of metallic glasses, Npj Comput Mater 4 (2018).
- [30] S.D. Zhang, Z.M. Wang, X.C. Chang, W.L. Hou, J.Q. Wang, Identifying the role of nanoscale heterogeneities in pitting behaviour of Al-based metallic glass, Corros. Sci. 53 (9) (2011) 3007–3015.
- [31] Y. Masumoto, A. Inoue, A. Kawashima, K. Hashimoto, A.P. Tsai, T. Masumoto, The effect of structural relaxation on the corrosion behavior of amorphous (Ni-Pd) 82si18 alloys, J. Non-Cryst. Solids 86 (1–2) (1986) 121–136.
- [32] U.K. Mudali, S. Baunack, J. Eckert, L. Schultz, A.J.J.O.A. Gebert, Compounds, pitting corrosion of bulk glass-forming zirconium-based alloys, J. Alloys Compd. 377 (1–2) (2004) 290–297
- [33] U. Koster, D. Zander, Triwikantoro, A. Rudiger, L. Jastrow, Environmental properties of Zr-based metallic glasses and nanocrystalline alloys, Scr. Mater. 44 (8–9) (2001) 1649–1654.
- [34] C.W. Chu, J.S.C. Jang, S.M. Chiu, J.P. Chu, Study of the characteristics and corrosion behavior for the Zr-based metallic glass thin film fabricated by pulse magnetron sputtering process, Thin Solid Films 517 (17) (2009) 4930–4933.
- [35] D. Zander, U.J.M.S. Köster, E. A, Corrosion of amorphous and nanocrystalline Zr-based alloys, Mater. Sci. Eng. A 375 (2004) 53–59.
- [36] S.G. Mayr, K. Samwer, Tailoring the surface morphology of amorphous thin films by appropriately chosen deposition conditions, J. Appl. Phys. 91 (5) (2002) 2779–2784
- [37] K. Khojier, H. Savaloni, E. Shokrai, Z. Dehghani, N.Z. Dehnavi, Influence of argon gas flow on mechanical and electrical properties of sputtered titanium nitride thin films, J Theor Appl Phys 7 (1) (2013).
- [38] J.P. Chu, C.Y. Wang, L.J. Chen, Q. Chen, Annealing-induced amorphization in a sputtered glass-forming film: in-situ transmission electron microscopy observation, Surf. Coat. Technol. 205 (8–9) (2011) 2914–2918.
- [39] W.C. Oliver, G.M. Pharr, An improved technique for determining hardness and elastic-modulus using load and displacement sensing indentation experiments, J. Mater. Res. 7 (6) (1992) 1564–1583.
- [40] G.M. Pharr, J.H. Strader, W.C. Oliver, Critical issues in making small-depth mechanical property measurements by nanoindentation with continuous stiffness measurement, J. Mater. Res. 24 (3) (2009) 653–666.
- [41] J.H. Chu, H.W. Chen, Y.C. Chan, J.G. Duh, J.W. Lee, J. Jang, Modification of structure and property in Zr-based thin film metallic glass via processing temperature control, Thin Solid Films 561 (2014) 38–42.

- [42] K.B. Kim, J. Das, F. Baier, M.B. Tang, W.H. Wang, J. Eckert, Heterogeneity of a Cu47.5Zr47.5Al5 bulk metallic glass, Appl. Phys. Lett. 88 (5) (2006).
- [43] P. Denis, S. Liu, H. Fecht, Growth mode transition in Au-based thin film metallic glasses, Thin Solid Films 665 (2018) 29–35.
- [44] Y. Liu, T. Fujita, A.E. Hirata, S. Li, H. Liu, W. Zhang, A. Inoue, M.J.I. Chen, Deposition of multicomponent metallic glass films by single-target magnetron sputtering, Intermetallics 21 (1) (2012) 105–114.
- [45] S.V. Ketov, R. Joksimovic, G. Xie, A. Trifonov, K. Kurihara, D.V.J.H. Louzguine-Luzgin, Formation of nanostructured metallic glass thin films upon sputtering, Heliyon 3 (1) (2017) e00228.
- [46] S. Qu, Y. Huang, W.D. Nix, H. Jiang, F. Zhang, K.C. Hwang, Indenter tip radius effect on the Nix-Gao relation in micro- and nanoindentation hardness experiments, J. Mater. Res. 19 (11) (2004) 3423–3434.
- [47] R. Yang, Q. Zhang, P. Xiao, J. Wang, Y.L. Bai, Two opposite size effects of hardness at real nano-scale and their distinct origins, Sci. Rep. 7 (2017).
- [48] A. Leyland, A. Matthews, On the significance of the H/E ratio in wear control: a nanocomposite coating approach to optimised tribological behaviour, Wear 246 (1–2) (2000) 1–11.
- [49] D.T.A. Matthews, V. Ocelik, J.T.M. de Hosson, Tribological and mechanical properties of high power laser surface-treated metallic glasses, Mat Sci Eng a-Struct 471 (1–2) (2007) 155–164.
- [50] J. Kim, H.S. Oh, W. Kim, P.-P. Choi, D. Raabe, E.S.J.A.M. Park, Modulation of plastic flow in metallic glasses via nanoscale networks of chemical heterogeneities, Acta Mater. 140 (2017) 116–129.
- [51] W.H. Wang, Dynamic relaxations and relaxation-property relationships in metallic glasses, Prog. Mater. Sci. 106 (2019).
- [52] A. Obeydavi, A. Shafyei, A. Rezaeian, P. Kameli, J.W. Lee, Microstructure, mechanical properties and corrosion performance of Fe44Cr15Mo14Co7C10BSSi5 thin film metallic glass deposited by DC magnetron sputtering, J. Alloys Compd. 527 (2020) 119718.
- [53] A. Caron, R. Wunderlich, D.V. Louzguine-Luzgin, G. Xie, A. Inoue, H.J. Fecht, Influence of minor aluminum concentration changes in zirconium-based bulk metallic glasses on the elastic, anelastic, and plastic properties, Acta Mater. 58 (6) (2010) 2004–2013.
- [54] N. Wang, J. Ding, P. Luo, Y. Liu, L. Li, F.J.M.R.L. Yan, Chemical variation induced nanoscale spatial heterogeneity in metallic glasses, Materials Research Letters 6 (12) (2018) 655–661.
- [55] J. Lee, M.-L. Liou, J.-G.J.S. Duh, C. Technology, The development of a Zr-Cu-Al-Ag-N thin film metallic glass coating in pursuit of improved mechanical, corrosion, and antimicrobial property for bio-medical application, Surf. Coat. Technol. 310 (2017) 214–222.
- [56] J.F. Archard, Contact and rubbing of flat surfaces, J. Appl. Phys. 24 (8) (1953) 981–988
- [57] M. Stern, A.L.J.J.o.t.e.s. Geary, Electrochemical polarization I. A theoretical analysis of the shape of polarization curves, J. Electrochem. Soc. 104(1) (1957) 56–63.
- [58] M.J. Duarte, A. Kostka, J.A. Jiménez, P. Choi, J. Klemm, D. Crespo, D. Raabe, F.U.J.A.m. Renner, Crystallization, phase evolution and corrosion of Fe-based metallic glasses: an atomic-scale structural and chemical characterization study, Acta Mater. 71 (2014) 20–30.
- [59] W.H. Jiang, F. Jiang, B.A. Green, F.X. Liu, P.K. Liaw, H. Choo, K.Q. Qiu, Electrochemical corrosion behavior of a Zr-based bulk-metallic glass, Appl. Phys. Lett. 91 (4) (2007).
- [60] F.F. Marzo, A.R. Pierna, M.M. Vega, Effect of irreversible structural relaxation on the electrochemical behavior of Fe78-xSi13B9Cr(x=3,4,7) amorphous alloys, J. Non-Cryst. Solids 329 (1–3) (2003) 108–114.
- [61] K. Asami, B.-P. Zhang, M. Mehmood, H. Habazaki, K.J.S.m. Hashimoto, Effects of nanoscale heterogeneity on the corrosion behavior of non-equilibrium alloys, Scr. Mater. 44 (8–9) (2001) 1655–1658.
- [62] W.C. Johnson, P. Zhou, A. Lucente, J.J.M. Scully, M.T. A, Composition profiles around solute-lean, spherical nanocrystalline precipitates in an amorphous matrix: implications for corrosion resistance, Metall. Mater. Trans. A 40 (4) (2009) 757-767
- [63] M. Mehmood, E. Akiyama, H. Habazaki, A. Kawashima, K. Asami, K. Hashimoto, The effect of heat treatment on the corrosion behavior of sputter-deposited aluminum-chromium alloys, Corros. Sci. 41 (3) (1999) 477–499.
- [64] K.D. Ralston, N. Birbilis, Effect of grain size on corrosion: a review, Corrosion-Us 66 (7) (2010).
- [65] J. Chen, J. Xiao, J. Poplawsky, F.M. Michel, C. Deng, W.J.C.S. Cai, The origin of passivity in aluminum-manganese solid solutions, Corros. Sci. (2020) 108749.
- [66] B. Sun, Y. Hu, D. Wang, Z. Zhu, P. Wen, W. Wang, C. Liu, Y.J.A.M. Yang, Correlation between local elastic heterogeneities and overall elastic properties in metallic glasses, Acta Mater. 121 (2016) 266–276.
- [67] D.D. Liang, X.S. Wei, T.C. Ma, B. Chen, H.R. Jiang, Y. Dong, J. Shen, Sliding tribocorrosion behavior of Fe-based bulk metallic glass under corrosive environments, J. Non-Cryst. Solids 510 (2019) 62–70.
- [68] A. Erdemir, A crystal chemical approach to the formulation of self-lubricating nanocomposite coatings, Surf. Coat. Technol. 200 (5–6) (2005) 1792–1796.
- [69] J. Chen, W.J. Cai, Effect of scratching frequency on the tribocorrosion resistance of Al-Mn amorphous thin films, Wear 426 (2019) 1457–1465.